Excited Interatomic Potential Energy Surfaces of Rb + He that correlate with Rb terms 5^{2}S through 7^{2}S

Journal:	*Physical Chemistry Chemical Physics*
Manuscript ID	CP-ART-09-2018-005550.R2
Article Type:	Paper
Date Submitted by the Author:	02-Nov-2018
Complete List of Authors:	Sharma, Amit; Wright State University, Department of Physics Weeks, David; Air Force Institute of Technology, Department of Engineering Physics

PCCP

ROYAL SOCIETY OF CHEMISTRY

ARTICLE TYPE

Cite this: DOI: 10.1039/xxxxxxxxxx

Excited Interatomic Potential Energy Surfaces of Rb + He that correlate with Rb terms 5^2S through 7^2S

Amit. R. Sharma*[a] and David E. Weeks[b]

Received Date
Accepted Date

DOI: 10.1039/xxxxxxxxxx

www.rsc.org/journalname

The excited state interatomic potential energy surfaces for Rb+He are computed at the spin-orbit multi-reference configuration interaction level of theory using all-electron basis sets of triple and quadruple-zeta quality that have been contracted for Douglas-Kroll-Hess (DKH) Hamiltonian and includes core-valence correlation. Davidson-Silver corrections (MRCI+Q) are employed to ameliorate size consistency error. An extrapolation of CASSCF energies is performed using the procedure of Karton and Martin whereas extrapolation of correlation energy is performed using an expression involving the inverse powers of $(l_{max}+1/2)$, the highest angular momentum value present in the basis set. The spin-orbit energies in the limit of complete basis set are obtained by replacing the energy eigenvalues in the spin-orbit matrix by the relativistic-corrected MRCI+Q energies extrapolated to the complete basis set limit. MRCI diabatic potential energy surfaces for a few selected $^2\Sigma$ states are calculated to study the general topology and avoided crossings and repulsive form of the 6s $^2\Sigma^+$ state. Important features of the potential energy surfaces are discussed with implications for alkali laser spectroscopy.

1 Introduction

Optically Pumped Alkali Lasers (OPAL) employ low concentrations of an alkali metal (M) vaporized in a rare gas (Rg) buffer where the alkali atoms are pumped on the D2 transition and then collide with rare gas buffer atoms. These collisions cause the alkali atoms to make a fine structure transition from the $^2P_{3/2}$ excited level to the $^2P_{1/2}$ level and then lase on the D1 transition[1–5]. The numerical simulation of an OPAL system requires a variety of input parameters that depend on excited interatomic potential energy surfaces including pressure broadened absorption cross sections used to model bandwidth overlap between the pump and the D2 transition, and fine-structure cross sections for the $^2P_{3/2} \rightarrow {}^2P_{1/2}$ transition[6,7]. This interest in M + Rg line shapes[8–13] and fine structure transition rates[14,15] has led to a number of recent efforts to compute M + Rg interatomic potential energy surfaces[16,17]. These efforts focused primarily on the interatomic potential surfaces that correlate in the limit of large interatomic separation to the $^2S_{1/2}$ ground state and the $^2P_{1/2}$ and $^2P_{3/2}$ excited states of the alkali atom that comprise the fundamental OPAL lasing cycle.

There is additional interest in the processes that populate alkali energy levels above the $^2P_{3/2}$ level since alkali atoms in these higher states are shifted out of the laser cycle and are susceptible to ionization that will degrade laser performance[5,18,19]. In particular, single photon absorption from the alkali 5P level to higher energy levels may become important at higher pump powers. For Rb, the D2 pump frequency is centered on $12,817\text{cm}^{-1}$. At twice this frequency the atomic Rb 7^2S level is detuned by 678cm^{-1} and the 5^2D level is detuned by 68cm^{-1}[20]. For these detunings, single photon absorption will occur in the far-wing of the pressure broadened line shape and may be enhanced by the presence of satellite features.

In a recent study, Dhiflaoui *et. al.*[22] have calculated Rb+He potential energy surfaces that include spin-orbit effects only for the low-lying molecular states (states that correlate with the 5 ^2S and 5 ^2P Rb levels), and, their study does not include spin-orbit effects for the high-lying states that correlate with Rb levels up to 7 ^2S. In their study, the total potential energy is calculated as the sum of core-core interaction between the Rb+ ion and He atom, plus, the interaction between the valence electron and the ionic system Rb+He, and, the spin-orbit interaction energy. The calculation of the adiabatic potential is reduced to finding a solution for the one-electron Schrödinger equation with potential terms involving the effective potential describing the interaction between the electron and the core derived from spectroscopic or scattering experimental data, and a long-range part, and

[a] *Department of Physics, Wright State University, Dayton, OH 45435, USA; E-mail: amit.sharma@wright.edu*

[b] *Department of Engineering Physics, Air Force Institute of Technology 2950 Hobson Way, WPAFB, OH USA 45433.*

† Electronic Supplementary Information (ESI) available: [details of any supplementary information available should be included here]. See DOI: 10.1039/cXCP00000x/

an l-dependent pseudopotential describing the short-range interaction.[21] Such an approach shows good agreement with experimental data as long as the electron-core interaction plays a major role in determining the adiabatic potentials. In addition, Dubourg *et. al.*[22] have observed that while the electron-core interaction approach results in good agreement between theory and experiment for Cs+He and Cs+Ar, the agreement is not as well established for Rb+He and Rb+Ar.

In this paper, we compute spin-free and spin-orbit interatomic potential energy surfaces of Rb + He that correlate in the limit of large internuclear separation to the atomic Rb 5 ^2S, 5 ^2P, 4 ^2D, 6 ^2S, 6 ^2P, 5 ^2D, and 7 ^2S levels. The calculations are performed at the spin-orbit multi-reference configuration interaction level of theory using all-electron basis sets developed by Hill and Peterson, which are of triple- and quadruple-zeta quality contracted for the Douglas-Kroll-Hess (DKH) Hamiltonian and include functions for the description of core-valence correlation[23]. An MRCI *posteriori* correction to estimate the contribution of the quadruple excitations due to Davidson (MRCI+Q) are employed to approximately restore size consistency up to the fourth order in perturbation series. A basis set extrapolation of CASSCF energies is performed using the procedure of Karton and Martin. Extrapolation of the correlation energy is performed separately using an expression involving the inverse powers of the highest angular momentum value present in the basis set[24]. The spin-orbit energies in the complete basis set limit (CBS) are obtained by replacing the energy eigenvalues in the spin-orbit matrix by extrapolated energy values that include Davidson- and relativistic-corrections. The 4s and 4p orbitals are doubly occupied in all configurations but these orbitals are correlated at the MRCI level through single and double excitations into the virtual orbitals. In addition to the inclusion of the outer-core correlation [valence + $(m-1)sp$], this study includes core-core correlation and core-valence correlation by a weighted approach.[23]

The paper is organized as follows. In section II we outline the computational approach and basis set extrapolation scheme used for computing the potential energy surfaces. The choice of active space and the rationale for augmenting basis sets with even-tempered functions is discussed in Section III. In Section IV, the newly computed potential energy surfaces are presented followed by satellite peak discussion for the Rb+He system. The diabatic transformation of adiabatic states is also discussed in Section IV followed by concluding remarks and summary are given in Sec. V.

2 Computational Approach

The electronic wave function of Rb+He is first determined with the multiconfiguration self-consistent field (MCSCF) approach[25,26]. The MCSCF wave function captures static correlation energy due to near degeneracy between different configurations,[27–29], whereas the remaining part of the correlation energy (dynamical) is obtained by augmenting the MCSCF wave function with all CSFs that differ by at most two molecular orbitals, namely the multireference single and double excitation configuration interaction (MRCI)[30–32]. Size-extensivity and size consistency of the CISD energies is improved by applying the multireference Davidson correction (MRCI+Q) to MRCI energies[33]. The energies are also corrected for relativistic effects using the 2nd-order Douglas-Kroll-Hess[34–36] method. The relativistic MRCI+Q spin-orbit energies are obtained by replacing the CI energy eigenvalues with MRCI+Q energies and diagonalizing the $\hat{H}_{el} + \hat{H}_{SO}$ using the Breit-Pauli (BP) operator on internally contracted CI wave functions. The result is known as the Davidson corrected spin-orbit (SO) matrix, and its diagonalization results in the relativistic corrected MRCI+Q spin-orbital energies.

Table 1 The Rb electronic configuration and corresponding Rb atomic terms, the He atomic terms, and Rb + He molecular terms

He atomic state	Rb electronic configuration [Ni-28] 4s2 4p6	Rb atomic state term ‡	Molecular term w/o SO
	$5s^1$	$^2S_{1/2}$	$^2\Sigma$
$^1S_{0,g}$	$5p^1$	$^2P_{1/2,3/2}$	$^2\Sigma$, $^2\Pi$
	$4d^1$	$^2D_{5/2,3/2}$	$^2\Sigma$, $^2\Pi$, $^2\Delta$
	$6s^1$	$^2S_{1/2}$	$^2\Sigma$
	$6p^1$	$^2P^o_{1/2,3/2}$	$^2\Sigma$, $^2\Pi$
	$5d^1$	$^2D_{3/2,5/2}$	$^2\Sigma$, $^2\Pi$, $^2\Delta$
	$7s^1$	$^2S_{1/2}$	$^2\Sigma$

The MCSCF active space for Rb+He molecular system is comprised of 19 A_1, 8 B_1, 8 B_2 and 3 A_2 occupied orbitals according to the complete active space (CAS) formulation in C_{2v} point group symmetry. The occupied orbitals include a total of 14 orbitals (28 electrons) comprising the Ni core, plus, 4s Rb orbital (A_1), 4p Rb orbital (A_1,B_1, and B_2), 5s Rb orbital (A_1), and, He 1s orbital (A_1) which constitutes Rb+He electronic ground state configuration (11 A_1, 4 B_1, 4 B_2 and 1 A_2). In addition to the Rb+He ground state configuration, the active space includes 8 A_1, 4 B_1, 4 B_2 and 2 A_2 Rb orbitals representing the 5p, 4d, 6s, 6p, 5d and 7s Rb orbitals. The inactive orbital space (doubly occupied) in the MCSCF calculation includes 10 A_1, 4 B_1, 4 B_2 and 1 A_2 orbitals which include 4s and 4p orbitals of Rb and 1s He orbital. This 19 closed-shell and 19 active orbitals active space results in 7 atomic states of Rb or 13 doublet molecular reference states as shown in Table 1.

The same active space is used to perform multireference configuration interaction singles and doubles (MRCISD) calculations[30–32] with the exception of the core orbital treatment. A total of 14 orbitals ($7A_1$, $3B_1$, $3B_2$ and $1A_2$) are treated as frozen-core orbitals in MRCI calculations. The frozen-core orbitals are doubly occupied in all configurations and are not correlated. In the present calculation, the 4s and 4p orbitals of Rb are doubly occupied in all configurations, but these orbitals are correlated at the MRCI level through single and double

‡ Superscript o means the parity $P = (-1)^{\sum_i l_i}$ for the term is odd (P = -1).

Table 2 The effect of inclusion of 4s and 4p orbitals in MCSCF and MRCI calculations calculated with aug-cc-pVTZ-DK2 basis set. The ✓ label indicates that the 4s and 4p orbitals form part of the active space in the MCSCF calculations, and, for MRCI calculations, the 4s and 4p electrons are correlated. The ✗ label indicates the 4s and 4p orbitals do not form part of the active space in the MCSCF calculation, and, the 4s and 4p orbitals are doubly occupied in all configurations and not correlated in the MRCI calculation.

Conf.	Term	J	Exp.	MCSCF ✗ MRCI ✗	ΔE	MCSCF ✗ MRCI ✓	ΔE	MCSCF ✓ MRCI ✓	ΔE
$4p^6\ 5s^1$	5^2S	1/2	0.0	0.0	0.0	0.0	0.0	0.0	
$4p^6\ 5p^1$	5^2P^o	1/2	12579.0	10702.6	1876.3	12222.5	356.5	12218.6	360.3
		3/2	12816.5	10852.5	1964.1	12415.4	401.1	12403.7	412.9
$4p^6\ 4d^1$	4^2D	5/2	19355.2	17529.2	1826.0	19158.9	196.3	19175.6	179.6
		3/2	19355.6	17517.5	1838.1	19170.6	185.1	19172.3	183.4
$4p^6\ 6s^1$	6^2S	1/2	20132.5	17743.4	2389.1	19634.5	498.0	19616.6	515.9

excitations into the virtual orbitals. The choice of closing the 4s and 4p Rb orbitals in the MCSCF calculation and correlating through single and double excitations in the MRCI calculations are based on the analysis of Rb atomic energy level calculations up to the 6S state as shown in Table 2. It is seen from Table 2 that the difference between calculated and experimental energy levels are in the range of 1800 cm^{-1} to 2000 cm^{-1} when 4s and 4p orbitals are doubly occupied in any reference configuration state functions (treated as inactive orbitals) in MCSCF calculation and uncorrelated in MRCI calculations. The agreement between experimental and calculated energies improves when 4s and 4p orbitals are constrained to be doubly occupied but are correlated at the MRCI level, as seen in Table 2. It is interesting to note that correlating 4s and 4p electrons at the MRCI level is sufficient and making 4s and 4p orbitals active at MCSCF level does not have any significant impact on the atomic level predictions. However, the computational cost dramatically increases when the MCSCF active space is increased by 4 orbitals. Therefore, the potential energy surface calculations presented in this work do not include 4s and 4p orbital in the active space but 4s and 4p Rb electrons are correlated at the MRCI level of theory.

Potential energy surfaces corresponding to the molecular terms in Table 1 are calculated in C_{2v} point group representation, wherein, the 7 $^2\Sigma$ states are of symmetry A_1, the 4 $^2\Pi$ states are comprised of B_1 and B_2 symmetry components, and, the two $^2\Delta$ states of symmetry A_1 and A_2, resulting in a total of 9 A_1 states, and, 4 B_1 and B_2, and 2 A_2 states. All calculations have been performed with the MOLPRO electronic structure program package[37].

2.1 COMPLETE BASIS SET EXTRAPOLATION OF SPIN-FREE ENERGIES

The calculated PES are corrected for basis set completeness by extrapolating the energy values to the complete basis set limit. The CASSCF energies (reference energy for MRCI calculations) are extrapolated using a two-parameter formula recommended by Karton and Martin[38],

$$E(l_{max}) = E_{CBS} + A(l_{max}+1)e^{-9\sqrt{l_{max}}} \quad (1)$$

where, l_{max} is the highest angular momentum value present in the basis set (3 for TZ and 4 for QZ), $E(l_{max})$ is the CASSCF energy calculated using a particular basis set, A is the fitting coefficient, and, E_{CBS} is the energy in the complete basis set limit. The correlation energy is extrapolated using a formula with inverse powers of the highest angular momentum value present in the basis set (l_{max}),

$$E(l_{max}) = E_{CBS} + A/\left(l_{max}+\frac{1}{2}\right)^4 \quad (2)$$

where E(l_{max}) is the MRCI or MRCI+Q correlation energy for a specific correlation consistent basis set characterized by a fixed value of l_{max}, and, E_{CBS} is the correlation energy corresponding to the complete basis set limit. The MRCI+Q correlation energy is calculated as the difference between MRCI+Q energy and CASSCF energy. The calculated energy values for specific basis sets are used for calculating the fitting coefficients in Eq. 1 and Eq. 2 using a least-squares approach where the coefficient E_{CBS} yields the extrapolated energy value. The total energy in the complete basis set limit is expressed as the sum of extrapolated CASSCF energy and extrapolated correlation energy.

3 Excited Atomic Energy Levels of Rb

Since the interatomic PESs presented in this work correlate with the Rb 5^2S through 7^2S levels, the performance of the all-electron basis sets is first assessed by computing Rb atomic levels up to 7^2S state at the MRCI+Q level of theory, including spin-orbit interactions, using all-electron correlation consistent basis sets from triple- to quadruple-zeta quality - developed by Hill and Peterson[23]. The calculated atomic energy levels with the cc-pVnZ-DK2 (n=T and Q), aug-cc-pVnZ-DK2 (n=T and Q), and, aug-cc-pwCVnZ-DK2 (n=T and Q) basis sets are presented with the purpose of comparing the performance of different basis sets for atomic excitation energies. It is found that the valence double-zeta basis set for Rb with augmenting functions is not large enough for orbital calculations up to 7^2S atomic level, and, all-electron quintuple-zeta quality basis sets have not yet been developed for the Rb atom; therefore, we restrict the discussion only to triple- and quadruple-zeta quality basis sets.

In Ref.[23], Hill and Peterson, assessed the accuracy of the basis sets through benchmark calculations at the coupled-cluster level of theory for atomic properties such as ionization potentials and electron affinities, and, molecular properties such as spectroscopic constants of homonuclear diatomics (M_2), the fluorides MF, and the hydrides, MH. The authors found that the outer-core correlation and augmentation of the basis sets with extra diffuse functions was vital for accurate calculation of the atomic thermodynamic properties, and, for the spectroscopic properties of diatomic molecules.

Table 3 Comparison of Rb atomic energy levels (cm^{-1}) with experimental values. Energies are calculated at MRCI+Q/Spin-Orbit level with aug-cc-pV[T,Q]Z-DK2 basis sets, abbreviated as "aVnZ-DK" (n=T and Q). ΔE represents the energy difference between experimental energy values and calculated values ($E_{exp} - E_{calc}$)

Conf.	Term	J	Exp.	aVTZ-DK	ΔE	aVQZ-DK	ΔE
$4p^6\ 5s^1$	5^2S	1/2	0.0	0.0	0.0	0.0	0.0
$4p^6\ 5p^1$	5^2P^o	1/2	12579.0	12223.7	355.3	11881.2	697.7
		3/2	12816.5	12412.4	404.1	12059.1	757.4
$4p^6\ 4d^1$	4^2D	5/2	19355.2	19169.4	185.8	18698.2	657.0
		3/2	19355.6	19165.1	190.5	18689.0	666.6
$4p^6\ 6s^1$	6^2S	1/2	20132.5	19615.1	517.4	19418.5	714.0
$4p^6\ 6p^1$	6^2P^o	1/2	23715.1	23133.6	581.5	22830.9	884.2
		3/2	23792.6	23189.2	603.4	22884.6	908.0
$4p^6\ 5d^1$	5^2D	3/2	25700.5	25332.6	367.9	25171.0	529.5
		5/2	25703.5	25334.8	368.7	25177.2	526.3
$4p^6\ 7s^1$	7^2S	1/2	26311.4	28724.8	-2413.4	26690.0	-378.5

Table 4 Comparison of Rb atomic energy levels (cm^{-1}) with experimental values. Energies are calculated at MRCI+Q/Spin-Orbit level with aug-cc-pwCV[T,Q]Z-DK2 basis sets. The basis sets abbreviated by awCVTZ-DK represents the aug-cc-pwCVTZ-DK2 basis for 2nd-order DKH

Conf.	Term	J	Exp.	awCVTZ-DK	ΔE	awCVQZ-DK	ΔE	awCVTZ-DK §	ΔE	awCVQZ-DK §	ΔE
$4p^6\ 5s^1$	5^2S	1/2	0.0	0.0	0.0	0.0	0.0	0.0	0.0	0.0	0.0
$4p^6\ 5p^1$	5^2P^o	1/2	12579.0	12439.1	139.9	12459.6	119.4	12431.8	147.2	12453.2	125.8
		3/2	12816.5	12638.6	178.0	12657.4	159.1	12631.2	185.3	12651.0	165.6
$4p^6\ 4d^1$	4^2D	5/2	19355.2	19346.3	16.4	19268.2	87.0	19340.9	14.3	19278.0	77.2
		3/2	19355.6	19338.8	9.3	19259.4	96.3	19334.1	21.6	19269.9	85.8
$4p^6\ 6s^1$	6^2S	1/2	20132.5	19865.4	267.1	19904.9	227.6	19867.9	264.6	19906.2	226.3
$4p^6\ 6p^1$	6^2P^o	1/2	23715.1	23439.3	275.8	23479.6	235.5	23432.9	282.2	23473.3	241.8
		3/2	23792.6	23499.8	292.8	23538.8	253.8	23493.0	299.6	23532.4	260.2
$4p^6\ 5d^1$	5^2D	3/2	25700.5	25585.1	115.4	25780.2	-79.6	25551.1	149.5	25552.5	148.1
		5/2	25703.5	25588.2	115.3	25784.4	-80.9	25553.5	150.0	25555.3	148.2
$4p^6\ 7s^1$	7^2S	1/2	26311.4	28682.0	-2370.6	27213.0	-901.6	26109.9	201.5	26067.8	243.6

The atomic energy levels calculated with cc-pVnZ-DK2 shows poor agreement, especially for the 5D and 7S atomic levels, which is not surprising given the lack of augmented diffuse functions which has been shown to be important in Ref.[23]. Differences of the order of a few thousand wavenumbers for 5D state and tens of thousands of wavenumbers for the 7S atomic level were observed and therefore we do not consider cc-pVnZ-DK2 basis sets further in our discussion.

The comparison of atomic energy levels calculated at MRCI+Q level of theory and aug-cc-pVnZ-DK2 basis set (abbreviated as "aVnZ-DK" (n=T and Q)) is presented in Table 3. It is seen that the calculated excitation energy values are smaller compared to the experimental values and the agreement between experiment and calculated energy is poor when a larger, quadruple-zeta basis set, is used. A large energy difference is observed for the 7^2S level with the aVTZ-DK basis set, whereas the addition of additional basis functions, (1s, 1p, 1d, 1f, 1g, 1h), from TZ to QZ improves the agreement of the 7^2S level when compared with the experimental value.

The Rb energy levels calculated with the aug-cc-pwCVnZ-DK basis sets (abbreviated as "awCVnZ-DK", n=T,Q) are shown in Table 4. The awCVnZ-DK basis sets have an added core function, and, include core-valence correlation effects using a weighted approach which has been shown to be important for the accurate calculation of thermodynamic and spectroscopic properties of diatomic molecules[23]. Comparing the aVTZ-DK energy values from Table 3 with awCVTZ-DK energy values from Table 4, it is seen that the inclusion of the outer-core electron correlation improves the agreement for all atomic levels with the exception of the 7^2S state, indicating the need for additional basis functions to represent higher lying 7^2S state. A similar improvement due to added core and core-valence correlation is seen between aVQZ-DK and awCVQZ-DK basis sets, as seen from Table 3 and Table 4. No systematic convergence with respect to zeta-level is observed for the awCVnZ-DK basis sets, wherein, the difference between experimental and calculated excitation energy is seen to decrease between TZ and QZ for some energy levels while the difference grows for other atomic levels. It is also seen from Table 3 and Table 4 that the TZ basis set is not large enough for accurate representation of the 7^2S state, and, the addition of additional basis functions from TZ to QZ improves the accuracy of the 7^2S state.

In addition to the above basis set calculations, the awCVnZ-DK basis sets were extended by adding one even-tempered diffuse function each angular momentum (SPDF type) with the mean ratio of successive exponents determined from the exponents of awCVnZ-DK basis set. It is seen from Table 4 that the addition of diffuse functions strongly affects the 7^2S energy level prediction, thus improving the accuracy of predicted excitation energy. We do not perform systematic converge study of the excitation energies with respect to diffuse functions, however, we observed that by continually increasing the number of shells of diffuse

§ basis set plus even-tempered basis functions

functions (using an even-tempered approach), ranging from one to three sets of diffuse shells, the excitation energies did not change by more than 1 cm^{-1} for all states, except for the 7^2S state. The change for the latter was approximately 24 cm^{-1}, indicating reasonable convergence with respect to the diffuse functions.

It is observed from Table 4 that the calculated excitation energies are systematically smaller compared to the experimental values which may be either due to the ground state being higher in energy, or due to the lowering of excited states, which may be the consequence of state-averaged MCSCF calculation; or a combination of both. To fully understand the origin of systematic difference, a detailed study is required which must consider the effects of - relativistic treatment for individual states, the number of states included in state averaging, the active space used, and, the effect of optimal orbitals for each state.

It is particularly interesting to make a note of the 4 $^2D_{5/2}$ and 4 $^2D_{3/2}$ atomic levels resulting from $4p^6$ $4d^1$ Rb electronic configuration and their fine-structure splitting which is about an order of magnitude smaller than those expected from the Landé factor[39,40]. Experimentally, the two levels are separated by about 0.4 cm^{-1} exhibiting anomalous inverted fine-structure splitting with 4 $^2D_{5/2}$ lower in energy, whereas, the fine-structure splitting is normal for the P states and also for the 5 ^2D state of Rb. It has been experimentally determined that the hyperfine splitting for 4 ^2D is also inverted[41,42]. Such inversion, in the limit where J is a good quantum number, the $J = L - 1/2$ lies above the $J = L + 1/2$ is also known to occur for the 3 ^2D states of sodium and 4 ^2D term of potassium. However, as seen from Table 3, the theoretical configuration interaction approach results in a "normal" spin-orbit splitting, with 4 $^2D_{3/2}$ lower than the 4 $^2D_{5/2}$ level for the aVnZ-DK basis sets. A similar "normal" spin-orbit splitting is seen in Table 4 for the awCVnZ-DK basis sets. The ordering of the 4 $^2D_{5/2}$ and 4 $^2D_{3/2}$ states will be important in the discussion of spin-orbit molecular states that correlate with these spin-orbit atomic levels.

The molecular potential energy surfaces of Rb+He presented in this work are calculated with the extended awCVnZ-DK basis sets and extrapolated to the complete basis set limit.

4 Results and Discussion

4.1 Potential Energy Surfaces

The adiabatic spin-free potential energy surfaces for Rb paired with He are shown in Figure 1 and Figure 2. The ground state, $X^2\Sigma^+$ molecular surface that correlates with the ^2S atomic level of Rb is found to be repulsive over the entire range of internuclear separation (R). The $A^2\Pi$ and $B^2\Sigma^+$ surfaces that correlate with the ^2P atomic level of Rb are shown in the upper panel of Figure 1. It is seen that the $A^2\Pi$ surface is attractive with a calculated well-depth of -202 cm^{-1} at an R-value of 5.65 bohr, beyond which, the potential becomes repulsive. The asymptotic value of the $A^2\Pi$ surface with respect to the asymptotic value of the $X^2\Sigma^+$, in the complete basis set, is 12,605 cm^{-1}, as shown in

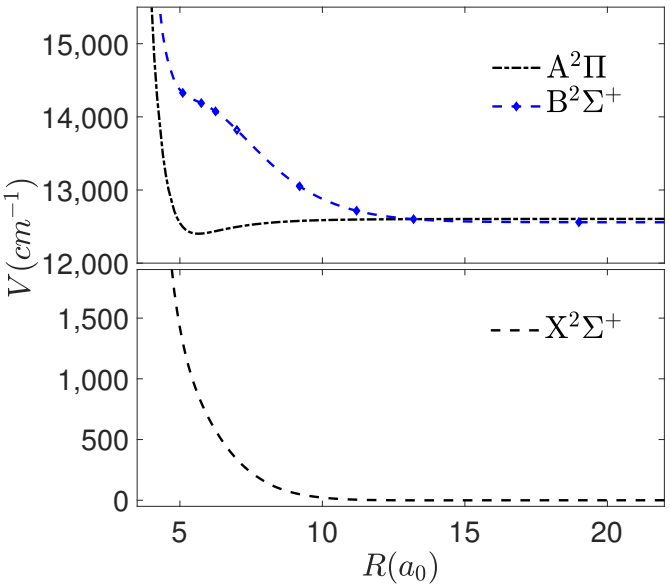

Fig. 1 The Rb+He molecular potential energy surfaces calculated using MRCI+Q level and extrapolated to the complete basis set limit from triple zeta(TZ) and quadruple zeta(QZ) basis sets. The lower panel shows the $X^2\Sigma^+$ surface that correlates with the atomic 5^2S Rb ground term ($4p^6 5s^1$). The upper panel shows the $A^2\Pi$ and $B^2\Sigma^+$ surfaces that correlate with the atomic 5^2P Rb term ($4p^6 5p^1$)

Figure 1.The $B^2\Sigma^+$ surface that correlates with the ^2P Rb atomic level is repulsive for all R-values and exhibits a shoulder in the range of R-values of 4 and 7 bohr.

A qualitative understanding of the shape of these potential energy surfaces can be obtained by analyzing the electron distribution along the internuclear axis of the alkali-noble-gas diatomic system. For the $X^2\Sigma^+$ molecular state, the Rb 5s electron is in the sσ orbital which allows for a closer approach and results in repulsive interaction with He atom at smaller R-values . For the, $B^2\Sigma^+$ state, the alkali electron is in pσ orbital which results in repulsive interaction with the approaching He closed shell s-orbital at larger R-values than the sσ orbital. The shoulder exhibited by the $B^2\Sigma^+$ potential energy surface could possibly be the result of lowered repulsion as the He atom passes through the region of the radial node of the pσ orbital or due to an avoided crossing with another electronic state of same symmetry. For the $A^2\Pi$ state the Rb atom wave-function has pπ character resulting in reduced repulsion along the internuclear axis, allowing closer approach before repulsive interaction dominates.

The molecular surfaces that correlate with the $4d^1$, $6s^1$, $6p^1$, $5d^1$ and $7s^1$ electronic configurations are shown in Figure 2 and the corresponding molecular terms are listed in Table 1. The $E^2\Sigma$, $C^2\Pi$ and $D^2\Delta$ surfaces that correlate with the ^2D Rb atomic level exhibit bonding strength ordering of $C^2\Pi > D^2\Delta > E^2\Sigma$ as shown in the lower panel of Figure 2. The $C^2\Pi$ surface has a well-depth of -417 cm^{-1} at R=5.45 bohr whereas the $D^2\Delta$ surface exhibits a minimum in the PES of -104 cm^{-1} at R=5.85 bohr, with an

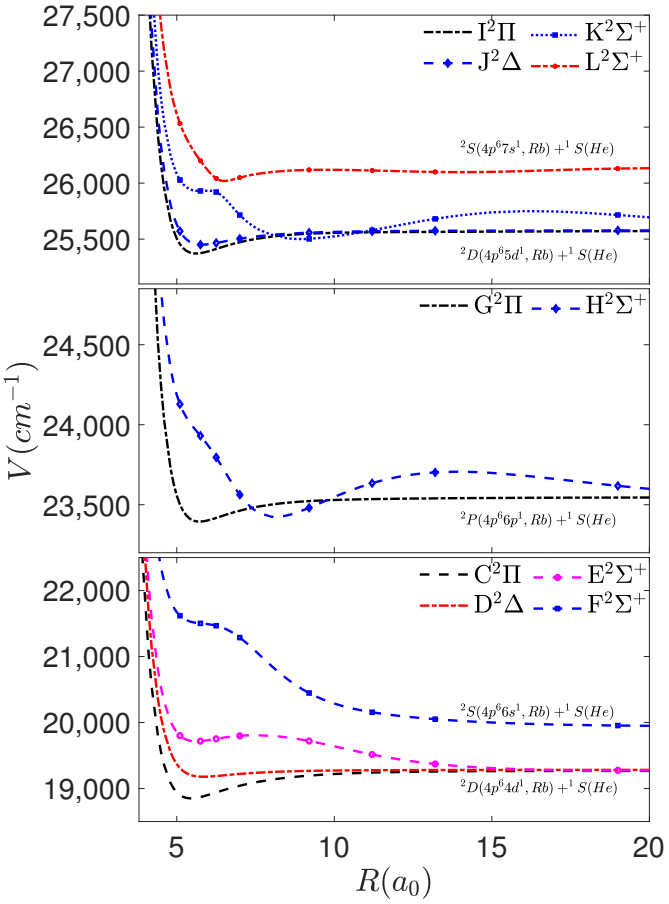

Fig. 2 The Rb+He molecular potential energy surfaces (PES) calculated using MRCI+Q level and extrapolated to the complete basis set limit from triple zeta(TZ) and quadruple zeta(QZ) basis sets. The PES correlate with $^2D(4p^6 4d^1)$ and $^2S(4p^6 6s^1)$ (lower panel); $^2P(4p^6 6p^1)$ (middle panel), and, $^2D(4p^6 5d^1)$ and $^2S(4p^6 7s^1)$ (upper panel)

asymptotic energy value of 19,283 cm^{-1}. These values are in agreement with reported well-depth of 523 cm^{-1} at R=5.85 bohr for the $C^2\Pi$ surface, and, 208 cm^{-1} at R=5.7 bohr for the $D^2\Delta$ state.[48] The $E^2\Sigma$ surface exhibits a shallow double-well potential with the potential energy value for all internuclear distance values higher than the asymptotic energy and a maximum of the saddle point of 533 cm^{-1} at R=7.4 bohr, with respect to its asymptotic value. The $E^2\Sigma$ surface exhibits a shallow minimum of 442 cm^{-1} at R=5.6 bohr, above the asymptotic energy value, which is in good agreement with well-depth value of 444 cm^{-1} at R=5.58 bohr reported by Dhiflaoui *et.al.*[48] The $F^2\Sigma$ surface resulting from the $6s^1$ Rb electronic configuration (^2S state) is also shown in the lower panel of Figure 2. The interaction of He atom with the diffuse 6s electron results in the repulsive potential energy surface along the He entrance channel of the $F^2\Sigma$ surface. The asymptotic value of the $F^2\Sigma$ surface in the complete basis set limit is calculated to be 19,944 cm^{-1}, as shown in Figure 2. A shoulder type structure is observed for the $F^2\Sigma$ surface around R=6 bohr, which is possibly due to avoided crossing with another electronic surface and will be further discussed later in the paper.

The molecular surfaces that correlate with the ^2P Rb term ($6p^1$ electronic configuration) are shown in the middle panel of Figure 2. The $G^2\Pi$ surface with an asymptotic value of 23,546 cm^{-1}, exhibits a shallow minimum at R=5.7 bohr with a well-depth of -151 cm^{-1}. The $H^2\Sigma$ surface exhibits a barrier to the entrance channel of He towards alkali atom. The inner minima on the $H^2\Sigma$ surface appears at R=8.2 bohr with well-depth of -113 cm^{-1}, below the asymptotic energy, whereas, the intermediate maxima appear at R=14.5 bohr, with the barrier height of 169 cm^{-1}, above the asymptotic energy value. These are in reasonable agreement with values reported by Dhiflaoui *et. al.*[48], with the reported well-depth value of 129 cm^{-1} at R=8.17 bohr for the $H^2\Sigma$ state, and, 225 cm^{-1} at R=5.66 bohr for the $G^2\Pi$ state. The $H^2\Sigma$ surface converges to the asymptotic value of the $G^2\Pi$ surface in the asymptotic limit.

Molecular surfaces that correlate with the ^2D and ^2S Rb terms ($5d^1$ and $7s^1$ electronic configuration, respectively) are shown in the upper panel of Figure 2. The $I^2\Pi$, $J^2\Delta$ surfaces are similar in character to the $C^2\Pi$, $D^2\Delta$ surfaces presented in the lower panel of Figure 2. The $I^2\Pi$ surface exhibits a minimum energy region (well-depth of -202 cm^{-1}) below the asymptotic energy at R=5.6 bohr, whereas, the $J^2\Delta$ surface monotonically decreases from the asymptotic region until R=5.75 bohr, with a minimum potential energy value of -128 cm^{-1} below the asymptotic energy. The $I^2\Pi$ asymptotic energy value is 25,574 cm^{-1}, which is good agreement with the fine-structure split $^2D_{3/2}$ and $^2D_{3/2}$ experimental energy values of 25,700.5 and 25,703.5 cm^{-1}, as shown in Table 4. Similar to the $H^2\Sigma^+$ surface, the $K^2\Sigma^+$ surface exhibits a saddle structure to the entrance channel, with a calculated barrier height of about 170 cm^{-1} for large internuclear separation (R $\approx$ 16 bohr), and, a minimum energy value of -79 cm^{-1} below the asymptotic value, around R=9 bohr. The well-depth, and internuclear separation values of the minimum for these high-lying states, are in reasonable agreement with the values reported by Dhiflaoui *et. al.*[48] The $L^2\Sigma^+$ potential energy surface shown in Figure 2 correlates with the $7s^1$ Rb term with an asymptotic energy value of 26,112 cm^{-1}. The $H^2\Sigma^+$ state and the $L^2\Sigma^+$ exhibit avoided crossing in the adiabatic representation around R=6.4 bohr indicating that the $H^2\Sigma^+$ state is repulsive for short nuclear distance, whereas, the $L^2\Sigma^+$ exhibit lowering of repulsion over small internuclear separations. The $K^2\Sigma$ surface converges to the asymptotic value of the 5^2D Rb term in the asymptotic limit.

4.2 Spin-Orbit Potential Energy Surfaces

The spin-orbit coupling is incorporated into the calculation using the Breit-Pauli (BP) operator in the basis of spin-free eigenfunctions. The spin-orbit CI potential energy surfaces that correlate with the $^2S_{1/2}$ and $^2P_{1/2,3/2}$ surfaces of the Rb atom, namely, the $X^2\Sigma^+_{1/2}$, $A^2\Pi_{1/2}$, $A^2\Pi_{3/2}$, and $B^2\Sigma^+_{1/2}$ surfaces are calculated at the MRCI+Q level of theory and extrapolated to the complete basis set size limit, are shown in Figure 3. The $X^2\Sigma^+_{1/2}$ ground electronic surface correlates to the $^2S_{1/2}$ atomic level of

Rb and it is found to be repulsive over all inter-nuclear distances which is similar to its spin-free counterpart. The $A^2\Pi_{1/2}$ surface with an asymptotic energy value of 12,456 cm^{-1}, correlates with the $^2P_{1/2}$ level of *Rb* and exhibits a small barrier beyond which the state turns attractive, resulting in a potential well minimum of -122 cm^{-1} with respect to its asymptotic energy value at R=5.65 bohr.

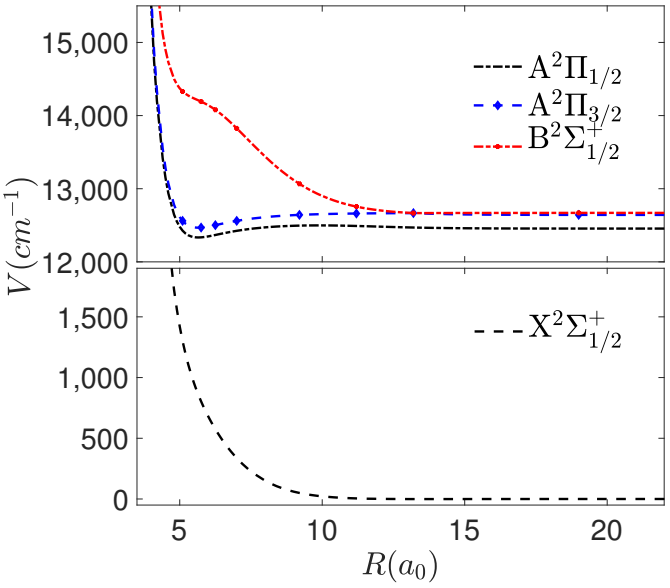

Fig. 3 The spin-orbit molecular potential energy surfaces (PES) calculated at MRCI+Q level and extrapolated to the complete basis set limit from all-electron triple-zeta(TZ) and quadruple-zeta(QZ) basis sets.

The $A^2\Pi_{3/2}$ and the $B^2\Sigma^+_{1/2}$ PESs are effectively degenerate in the asymptotic limit with an energy value of 12,670 cm^{-1}, and correlate to the $^2P_{3/2}$ level of *Rb*. As the internuclear separation decreases the molecular states diverge, with the $B^2\Sigma^+_{1/2}$ surface becoming repulsive and the $A^2\Pi_{3/2}$ surface becoming attractive with a well-depth of -175 cm^{-1} at R=5.65 bohr. The $B^2\Sigma^+_{1/2}$ surface exhibits a shoulder over a range of R=5-7 bohr which is possibly due to the lowering of repulsion as the He atom passes through the radial node of the pσ-orbital of the Rb atom. The spin-orbit splitting between $B^2\Sigma^+_{1/2}$ and the $A^2\Pi_{1/2}$ surfaces in the asymptotic limit is calculated to be 205 cm^{-1} with is in good agreement with experimentally measured splitting between $^2P_{1/2,3/2}$ of 237.5 cm^{-1} [20].

The well-depth, D_e (cm^{-1}), and equilibrium separations, r_m, of the $X^2\Sigma^+_{1/2}$, $A^2\Pi_{1/2}$, $A^2\Pi_{3/2}$, and $B^2\Sigma^+_{1/2}$ states calculated in the present work are presented in Table 5. The calculated values are also compared with various theoretical estimates, [16,17,21,43–50] that have been calculated using a variety of different approaches - ranging from wavefunction based *ab initio* methods [16,17,43,45,50] and DFT based approach [44], semi-classical perturbation theory approach [21], to an approach of model potential generation [46,49] where the problem is reduced to core-core interaction and one-electron-core interaction, [48] with assist from long-range dispersion coefficients in some studies. [47]

It is noted from Table 5 that the wavefunction based *ab initio* methods generate similar well-depth and equilibrium separation values, wheres the DFT approach and model-potential approach overestimate the well-depths for all states. It has been shown by Blank *et. al.* [17] that the well-depth values of the $A^2\Pi_{1/2}$ and $A^2\Pi_{3/2}$ states strongly depend on the quality of the basis set, and increasing the basis set size results in a deeper well and smaller equilibrium position; and, the higher order effects such as basis-set superposition errors results in significant change in the predicted well-depth and equilibrium position values. The present values are in good agreement with recent studies [17] based on a similar level of theory.

The spin-orbit surfaces that correlate with the $^2D_{3/2,5/2}$ and $^2S_{1/2}$ Rb terms are shown in the lower panel of Figure 4. The $C^2\Pi$ state splits into $C^2\Pi_{1/2}$ and $C^2\Pi_{3/2}$ whereas the $D^2\Delta$ splits into $D^2\Delta_{3/2}$ and $D^2\Delta_{5/2}$ state. The $E^2\Sigma$ results in $E^2\Sigma_{1/2}$ spin-orbit state which correlates to the $^2D_{5/2}$ Rb level. The $C^2\Pi_{1/2}$ and $C^2\Pi_{3/2}$ exhibit a small splitting of approximately 0.7 cm^{-1} ar R=14.5 bohr which only marginally increases with decreasing R-value with an overall splitting of less than a wavenumber. The $D^2\Delta_{3/2}$ and $D^2\Delta_{5/2}$ exhibit an overall splitting of approximately 9.6 cm^{-1} with a splitting of 8.3 cm^{-1} around the $D^2\Delta$ minimum at R=5.8 bohr. The $C^2\Pi_{1/2}$ exhibits a minimum of -405 cm^{-1} at R=5.45 bohr, which is also the case for the $C^2\Pi_{3/2}$ state as the two states are nearly degenerate. The $D^2\Delta_{3/2}$ and $D^2\Delta_{5/2}$ states exhibit a minimum with well-depth of -97 cm^{-1} at R=5.85 bohr. The $F^2\Sigma_{1/2}$ shown in the lower panel of Figure 4 correlates with $^2S_{1/2}$ Rb state resulting from $6s^1$ electronic configuration. The $F^2\Sigma_{1/2}$ is repulsive with a shoulder feature indicating avoided crossing with possibly another $^2\Sigma$ state, at short internuclear separation value.

The middle panel of Figure 4 shows the spin-orbit molecular surfaces that correlate with $^2P^o_{1/2,3/2}$ Rb terms. Similar to the $A^2\Pi_{1/2,3/2}$ and the $B^2\Sigma^+_{1/2}$ surfaces shown in Figure 3, the $G^2\Pi$ surface splits into $G^2\Pi_{1/2}$ and $G^2\Pi_{3/2}$ spin-orbit surfaces, whereas the $H^2\Sigma^+$ surface results in $H^2\Sigma_{1/2}$ surface. The $G^2\Pi_{1/2}$ and $H^2\Sigma_{1/2}$ molecular surfaces have an asymptotic energy value of 23,504 and 23,566 cm^{-1} (split by 62 cm^{-1}), respectively, which is good agreement with the $^2P^o_{1/2,3/2}$ Rb atomic levels of 23,715.1 and 23,792.6 cm^{-1} (split by 77.5 cm^{-1}). The $H^2\Sigma_{1/2}$ surface exhibits a barrier in the entrance channel which is similar to the spin-free $H^2\Sigma$ surface discussed before, it crosses the $G^2\Pi_{3/2}$ surface in the range or R=7.5-10 bohr, and converges to the asymptotic value of the $G^2\Pi_{3/2}$ surface in the asymptotic limit. Due to the lowering of point-group symmetry in the spin-orbit Hamiltonian, the $H^2\Sigma$ and $G^2\Pi$ have same symmetry which results in root flipping in the crossing region, which in turn, results in an unphysical dip in the $G^2\Pi_{1/2}$ state as seen in Figure 4. The root flipping between $G^2\Pi_{3/2}$ and $H^2\Sigma_{1/2}$ has been corrected in Figure 4,however, the $G^2\Pi_{1/2}$ has not been altered.

Table 5 The well-depth D_e (cm^{-1}) and equilibrium positions r_{min} (a_0) for the $X^2\Sigma^+_{1/2}$, $A^2\Pi_{1/2}$, $A^2\Pi_{3/2}$, and $B^2\Sigma^+_{1/2}$ electronic states. The table also includes barrier height and its position for the $A^2\Pi_{1/2}$ state.

Studies	$X^2\Sigma^+_{1/2}$	$A^2\Pi_{1/2}$		$A^2\Pi_{3/2}$	$B^2\Sigma^+_{1/2}$
	$D_e[r_{min}]$	$D_e[r_{min}]$	barrier [r]	$D_e[r_{min}]$	$D_e[r_{min}]$
Present	0.6 [14.5]	122 [5.65]	42.8 [9.9]	175 [5.65]	3.1 [13.4]
Hirano *et. al.*[43]	-	102.1[6.1]	26.5 [10.0]	176.8 [6.1]	-
Zbiri *et. al.*[44]	-	276 [6.1]	-	276 [6.1]	-
Pascale[21]	-	134 [6.25]	-	134 [6.25]	-
Chattopadhyay[45]	2.19 [14.5]	44 [6.4]	-	65.8 [6.4]	-
Patil[46]	1.02 [13.9]	-	-	-	-
Cvetko *et. al.*[47]	1.02 [13.9]	-	-	-	-
Dhiflaoui *et. al.*[48]	3.0 [12.8]	205 [5.6]	-	279 [5.6]	1.0 [20.04]
Kleinekathöfer *et. al.*[49]	0.81 [14.2]	-	-	-	-
Bouhadjar *et. al.*[50]	8.56 [12.4]	101.1 [5.9]	-	157.6 [5.9]	1.47 [20.6]
Blank *et. al.*[16]	8.7 [12.5]	95.9 [5.9]	20.0 [10.4]	159.1 [5.9]	0.3 [19.8]
Blank *et. al.*[17]	0.9 [14.4]	122.0 [5.7]	41.2 [10.0]	188.4 [5.7]	-

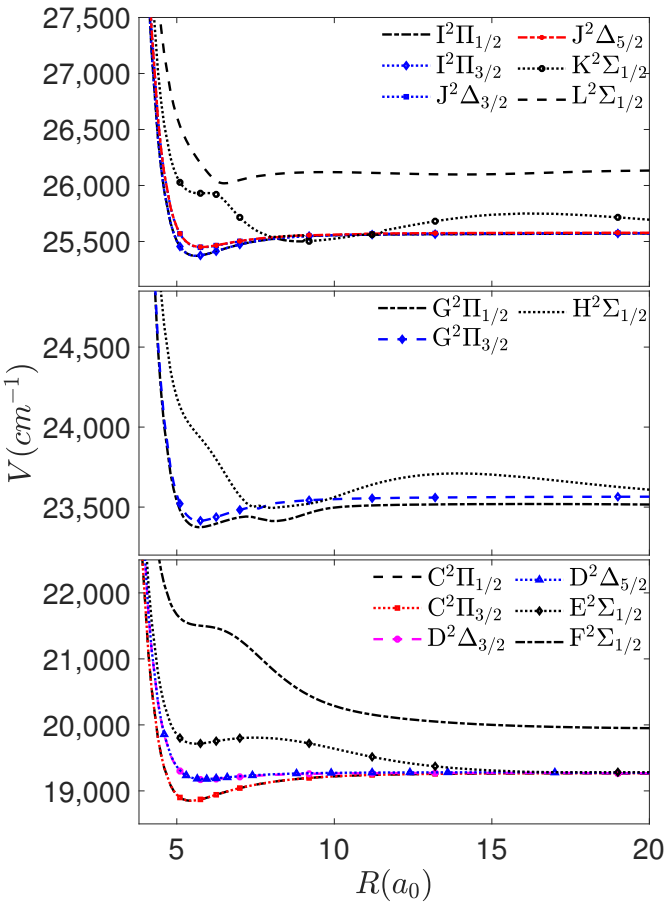

Fig. 4 The spin-orbit molecular potential energy surfaces (PES) calculated at MRCI+Q level and extrapolated to the complete basis set limit from all-electron triple-zeta(TZ) and quadruple-zeta(QZ) basis sets.

Finally, the spin-orbit molecular states that correlate with the $^2D_{3/2,5/2}$ and $^2S_{1/2}$ Rb atomic states are presented in the upper panel of Figure 4. The $I^2\Pi_{1/2}$ and $J^2\Delta_{3/2}$ correlate with $^2D_{3/2}$, whereas, the $I^2\Pi_{3/2}$, $J^2\Delta_{5/2}$ and $K^2\Sigma_{1/2}$ correlate with $^2D_{5/2}$ Rb level. The $^2\Pi$ and $^2\Delta$ spin-orbit states are similar in character to the $C^2\Pi$ and $D^2\Delta$ states discussed earlier with them being attractive in nature, and a minimum of approximately -202 cm^{-1} for the $^2\Pi$ state and -127 cm^{-1} for the $^2\Delta$, spin-orbit components with an asymptotic value of 25,574 cm^{-1} for the $I^2\Pi_{1/2}$ state. The $I^2\Pi_{1/2}$ and $I^2\Pi_{3/2}$ states, and the $J^2\Delta_{3/2}$ and $J^2\Delta_{5/2}$, are nearly degenerate with each other and are indistinguishable due to the scale of the plot in Figure 4.

The $K^2\Sigma_{1/2}$ surface exhibits a large barrier in the entrance channel with a barrier height of 170 cm^{-1}, and has a minimum which is lower than the $I^2\Pi$ and $J^2\Delta$ surfaces which results in the crossing of the $K^2\Sigma_{1/2}$ surface near an internuclear separation value of 11 bohr. The $K^2\Sigma_{1/2}$ surface is repulsive for the shorter Rb+He separation values, and exhibits an avoided crossing with the $L^2\Sigma^+_{1/2}$ surface. The $K^2\Sigma_{1/2}$ surface converges to the asymptotic value of the $I^2\Pi$ and $J^2\Delta$ surfaces at larger values of R. The asymptotic energy value of the $L^2\Sigma^+_{1/2}$ surface as shown in Figure 4 is 26,112 cm^{-1}, which is in good agreement with the experimentally measured value of 26,311.4 cm^{-1} for the $^2S_{1/2}$ atomic Rb level.

4.3 Satellite Peak

For the Rb+He system, the location, height and shape of the satellite peak of the rubidium D2 line is strongly dependent on the difference potential of the $A^2\Pi_{3/2}$ and $B^2\Sigma^+_{1/2}$ molecular states with respect to the ground electronic state, since both of these excited states have asymptotic limits that correspond to the $^2P_{3/2}$ state of Rb atom[13,17]. In an earlier study, we calculated the Rb+He potential energy surfaces with relativistic effective core potential (ECP) basis sets ranging from double-zeta, triple-zeta to quadruple-zeta quality, and, extrapolated the potential energy surfaces to the complete basis set limit[17]. The prediction of satellite peak position is a function of the extremum of the difference potential and it was shown in Ref.[17] that the satellite line position prediction systematically converges with the valence quality of the basis set.

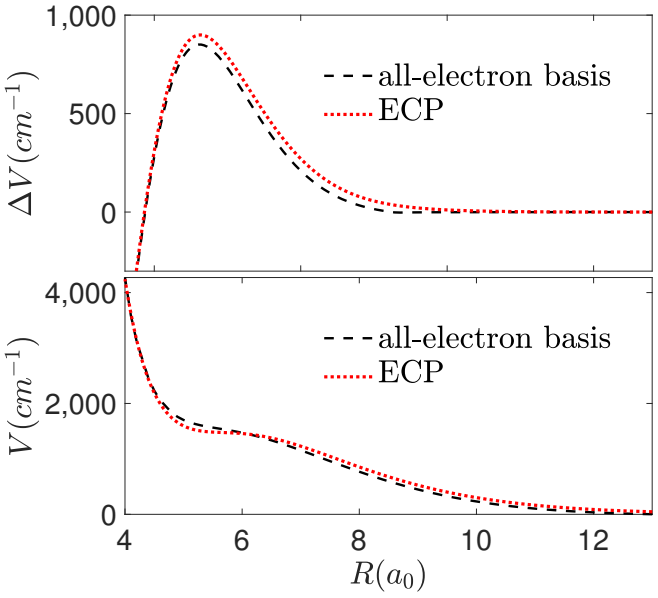

Fig. 5 The upper panel shows the difference potential between the $B^2\Sigma^+_{1/2}$ and $X^2\Sigma^+_{1/2}$ PECs calculated with the all-electron basis sets (labeled as all-elec) and with effective core potential basis sets (labeled as ECP) [17]. The lower panel shows the $B^2\Sigma^+_{1/2}$ molecular state calculated with the all-electron basis sets compared to the $B^2\Sigma^+_{1/2}$ state calculated with the ECP basis sets [17].

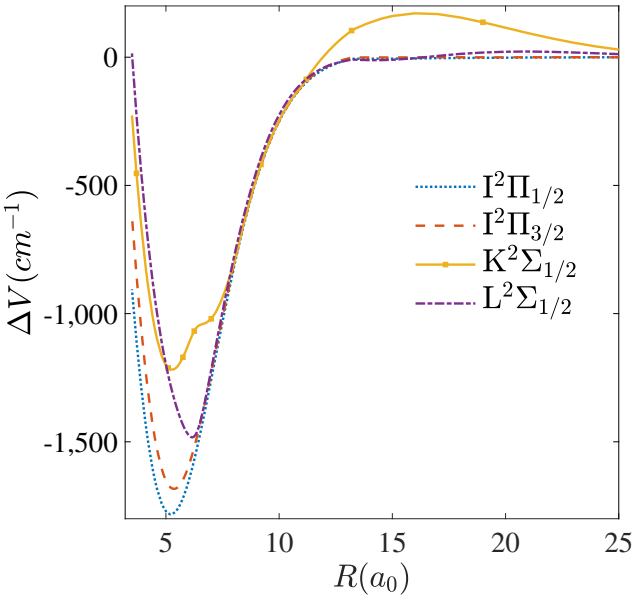

Fig. 6 The difference potential between the $B^2\Sigma^+_{1/2}$ state and $I^2\Pi_{1/2}$, $I^2\Pi_{3/2}$, $K^2\Sigma_{1/2}$, $L^2\Sigma_{1/2}$ PECs calculated with the all-electron basis sets.

The $B^2\Sigma^+_{1/2}$ molecular state, and, the difference potential between $B^2\Sigma^+_{1/2}$ and $X^2\Sigma^+_{1/2}$ state, calculated with the all-electron basis sets and extrapolated to the complete basis set limit is compared with corresponding energy values calculated with the DZ, TZ and QZ ECP basis sets and extrapolated to the complete basis set limit from Ref. [17]. It is seen from Figure 5 that the shoulder on $B^2\Sigma^+_{1/2}$ molecular state is less pronounced for the all-electron basis set and the $B^2\Sigma^+_{1/2}$, $X^2\Sigma^+_{1/2}$ difference potential is nearly identical for the two different types of basis sets with the exception of a small lowering of the extremum of the difference potential. The satellite line position with respect to the experimental line center, calculated with the present all-electron potential energy surfaces is 732 nm (experimental value 735 nm). Comparing with the predicted satellite line position from Ref. [17] the current prediction is a modest improvement over ECP basis set values.

The line centers of transitions that result in the depopulation of the $^2P_{3/2}$ state by pumping to the $^2D_{3/2}$ and $^2S_{1/2}$ lies at 776.1 nm and 741 nm, respectively. The satellite feature for these transitions can be calculated from the extremum of the difference potential between the $B^2\Sigma^+_{1/2}$ state and $I^2\Pi_{1/2}$, $I^2\Pi_{3/2}$, $K^2\Sigma_{1/2}$, $L^2\Sigma_{1/2}$ molecular states shown in Figure 6. The satellite peak resulting from the extremum of the difference potential for the $B^2\Sigma^+_{1/2} \rightarrow I^2\Pi_{3/2}$ transition appears at 854 nm, whereas, the satellite peak for the $B^2\Sigma^+_{1/2} \rightarrow L^2\Sigma_{1/2}$ transition appears at 832 nm. These calculations indicate that the satellite peaks are redshifted and lie below the pump and lase frequencies. As a result, transitions from the Rb $^2P_{3/2}$ level to the 5D and 7S levels will be governed by the far-wing amplitude of the line shape in the region between the line center and the redshifted satellite peak.

4.4 Diabatic structure of potential energy surfaces

The adiabatic excited states for Rb+He, especially the $^2\Sigma^+$ states shown in Figure 1 and Figure 2 exhibit shoulder type features, double well potential and possibly avoided crossing (or at least strong mixing) with other electronic states. The $E^2\Sigma^+$ state shown in Figure 2 exhibits shoulder which is indicative of avoided crossing with a state of the same symmetry (not clearly seen due to the scale of the plot) and similar features are observed for $F^2\Sigma^+$ states and for high-lying $K^2\Sigma^+$ and $L^2\Sigma^+$ states. In an effort to gain a qualitative understanding of the mixing of the electronic state we diabatized the first four $^2\Sigma^+$ states using the DDR procedure available in MOLPRO to generate quasi-diabatic states and energies for MRCI wavefunctions [37].

The diabatization procedure involves rotation of CASSCF orbitals to maximize the overlap with orbitals at reference geometry where the adiabatic and diabatic states are preferably identical, and, calculation of transition densities at displaced geometries and transition densities between displaced and reference geometries using wavefunctions calculated at respective geometries. The active space chosen for computing diabatic potential energy surfaces includes the 4f Rb orbital in addition to the active space described in Section 2. The 4s and 4p orbitals are treated as core orbitals in MRCI calculation. The diabatic potential energy surfaces are calculated using the aug-cc-pVTZ-DK2 basis set for Rb and aug-cc-pVTZ for He atom, without any additional diffuse functions and no basis set extrapolation is performed; therefore, the diabatic surfaces presented here are to be considered as preliminary qualitative

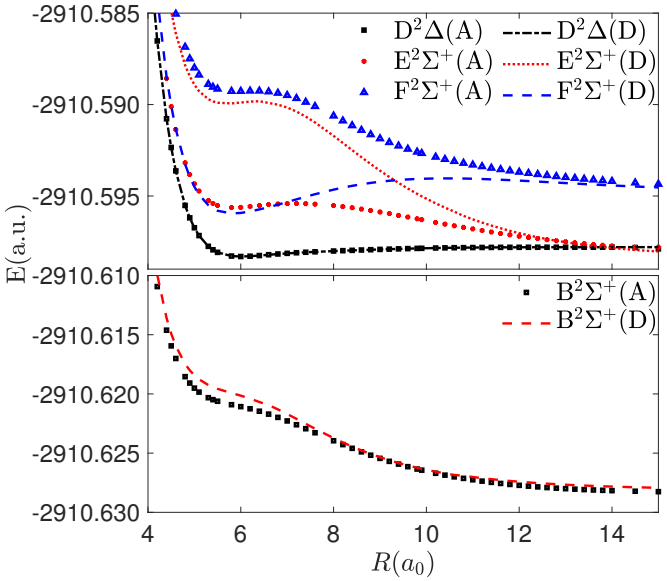

Fig. 7 The adiabatic (A) and diabatic (D) potential energy surfaces of the $B^2\Sigma^+$ state for Rb+He (lower panel). The upper panel shows adiabatic and diabatic potential energy surfaces for $D^2\Delta$, $E^2\Sigma^+$ and $F^2\Sigma^+$ states.

analysis, and a detailed study of the Rb+He diabats is planned for future.

The adiabatic and diabatic potential energy surfaces of four A_1 states are shown in Figure 7. It is seen that the diabatic potential energy surfaces tend to the adiabatic surfaces away from the crossing region, and are smooth in regions of crossings and avoided crossings. The diabatic $B^2\Sigma^+$ potential energy surface shown in the lower panel of Figure 7 is nearly identical to the adiabatic surface except for small deviation around the shoulder region. The upper panel shows the adiabatic and diabatic potential energy surfaces for $D^2\Delta$, $E^2\Sigma^+$, and $F^2\Sigma^+$ states. The $D^2\Delta$, adiabatic and diabatic surfaces are nearly identical, indicating little to no mixing of this state with the other $^2\Sigma$ states. The $E^2\Sigma^+$ and $F^2\Sigma^+$ states exhibit strong mixing with the diabatic $E^2\Sigma^+$ being strongly repulsive and crossing $F^2\Sigma^+$ state around R=9.3 bohr. It is seen that the diabatic $E^2\Sigma^+$ exhibits a shoulder in the range of 5 to 7.5 bohr indicating that the $E^2\Sigma^+$ state is repulsive in this region and the shoulder is formed due to avoided crossing with a higher energy excited state of same symmetry.

The diabatization of the $F^2\Sigma^+$ (6s $^2\Sigma^+$) shows that this state is less repulsive than the adiabatic state which is in agreement with the experimental determination of Dubourg *et. al.*[22], who found that the 6s $^2\Sigma^+$ adiabatic potential energy curves determined by the *l*-dependent potentials[21] were too repulsive in the 7-12 bohr region. A qualitative comparison of the experimentally determined potential energy[22] for the 6s $^2\Sigma^+$ state agrees with the present adiabatic and diabatic potential energy curve, shown in Figure 7.

5 Conclusions

Interatomic potential energy surfaces of Rb + He that correlate in the limit of large internuclear separation to the atomic Rb 5 ^2S, 5 ^2P, 4 ^2D, 6 ^2S, 6 ^2P, 5 ^2D, and the 7 ^2S levels are computed at the spin-orbit multi-reference configuration interaction level of theory. All-electron basis sets contracted for the Douglas-Kroll-Hess (DKH) Hamiltonian at triple- and quadruple-zeta quality are used for the calculations[23]. A Davidson correction is applied, and basis set extrapolation is performed to obtain interatomic potential energy surfaces in the CBS limit that include spin-orbit effects. These potential energy surfaces are used to explore the diabaticity several $^2\Sigma$ potential energy surfaces.

Difference potentials between the $B^2\Sigma^+_{1/2}$ potential energy surface and the $I^2\Pi_{1/2}$, $I^2\Pi_{3/2}$, $K^2\Sigma_{1/2}$, and $L^2\Sigma_{1/2}$ potential energy surfaces are computed and their extrema are used to estimate the location of satellite peaks of the line shape associated with transitions from the Rb $^2P_{3/2}$ level to the higher lying Rb 5^2D and 7^2S levels. The line centers of these transitions lie just above the pump and lasing frequencies and the large shoulder on the $B^2\Sigma^+_{1/2}$ potential energy surface causes the satellite peaks to be redshifted below the pump and lasing frequencies. As a result, transitions from the Rb $^2P_{3/2}$ level out of the lasing cycle into the 5D and 7S levels will be governed by the amplitude of the line shape between line center and the redshifted satellite peaks. Finally, it is worth noting that the barriers exhibited by both the $H^2\Sigma^+_{1/2}$ and $K^2\Sigma^+_{1/2}$ potential energy surfaces at large $R \approx 15$ bohr will increase the effective radius of Rb atoms during a collision and may give rise to anomalously large broadening coefficients for transitions involving these surfaces.

6 SUPPLEMENTARY MATERIAL

The spin-free and spin-orbit potential energy surfaces reported in this work are offered for public distribution as tabulated plain text files. The MCSCF energies are distributed for the MRCI and MRCI+Q level correlation energy calculations with aug-cc-pwCVnZ-DK2 (n=T and Q) basis sets. Tables for MRCI/spin-orbit and MRCI+Q/spin-orbit energies calculated with aug-cc-pwCVnZ-DK2 (n=T and Q) basis sets are also reported in the supplementary material. The MRCI+Q/spin-orbit energies extrapolated to the complete basis set limit as described in this work is included†.

Conflicts of interest

There are no conflicts to declare.

Acknowledgements

The authors wish to thank Prof. Kirk Peterson for valuable suggestions and help with the basis sets used in the present work. Generous support for A.R.S by the National Science Foundation (NSF) (MRI Award #1531923) is greatly appreciated. We are thankful to the NSF for the computational resources that were used for this research. A.R.S would also like to acknowledge the funding provided by Wright State University. The work is also supported in part by the Air Force Institute of Technology in the

form of summer fellowship through ORISE.

References

1 W. Krupke, R. Beach, V. Kanz and S. Payne, *Optics Letters*, 2003, **28**, 2336.

2 R. J. Beach, W. F. Krupke, V. K. Kanz and S. A. Payne, *J. Opt. Soc. Am. B*, 2004, **21**, 2151.

3 B. V. Zhdanov, T. Ehrenreich and R. J. Knize, *Opt. Commun.*, 2006, **260**, 696.

4 R. H. Page, R. J. Beach, V. K. Kanz and W. F. Krupke, *Opt. Lett.*, 2006, **31**, 353.

5 B. V. Zhdanov, J. Sell and R. J. Knize, *Electron. Lett.*, 2008, **44**, 582.

6 G. D. Hager and G. Perram, *Applied Physics B*, 2010, **101**, 45–56.

7 G. D. Hager and G. P. Perram, *Applied Physics B*, 2013, **112**, 507–520.

8 W. S. Miller, C. A. Rice, G. D. Hager, M. D. Rotondaro, H. Berriche and G. P. Perram, *J. Quant. Spectrosc. Radiat. Transfer*, 2016, **184**, 118–134.

9 W. S. Miller, C. A. Rice and G. P. Perram, *J. Quant. Spectrosc. Radiat. Transfer*, 2018, **206**, 151–156.

10 G. Pitz, D. Wertepny and G. Perram, *Phys. Rev. A*, 2009, **80**, 062718.

11 G. Pitz, C. Fox and G. Perram, *Phys. Rev. A*, 2010, **82**, 042502.

12 G. D. Hager, G. E. Lott, A. J. Archibald, L. Blank, D. E. Weeks and G. P. Perram, *J. Quant. Spectrosc. Radiat. Transfer*, 2014, **147**, 261–273.

13 L. Blank and D. E. Weeks, *Phys. Rev. A*, 2014, **90**, 022510.

14 C. D. Lewis and D. E. Weeks, *J. Phys. Chem. A*, 2017, **121**, 3340–3351.

15 B. Eshel, J. A. Cardoza, D. E. Weeks and G. P. Perram, *Phys. Rev. A*, 2017, **95**, 042708.

16 L. Blank, G. S. Kedziora and D. E. Weeks, *J. Chem. Phys.*, 2012, **136**, 124315.

17 L. A. Blank, A. R. Sharma and D. E. Weeks, *Physical Review A*, 2018, **97**, 032705.

18 R. Knize, B. Zhdanov and M. Shaffer, *Opt. Express*, 2011, **19**, 7894–7902.

19 A. Wallerstein, G. Perram and C. A. Rice, Solid State Lasers XXVII: Technology and Devices, 2018, p. 105112J.

20 2011, Y. Ralchenko, A. E. Kramida, J. Reader, and NIST ASD Team, NIST Atomic Spectral Database (ver. 4.1.0), (http://physics.nist.gov/asd3) National Institute of Standards and Technology, Gaithersburg, MD.

21 J. Pascale, *Phys. Rev. A*, 1983, **28**, 632.

22 I. Dubourg, M. Ferray, J. P. Visticot and B. Sayer, *Journal of Physics B: Atomic and Molecular Physics*, 1986, **19**, 1165.

23 J. G. Hill and K. A. Peterson, *The Journal of Chemical Physics*, 2017, **147**, 244106.

24 D. Feller, K. A. Peterson and J. Grant Hill, *The Journal of Chemical Physics*, 2011, **135**, 044102.

25 H.-J. Werner and P. J. Knowles, *J. Chem. Phys.*, 1985, **82**, 5053.

26 P. J. Knowles and H.-J. Werner, *Chem. Phys. Lett.*, 1985, **115**, 259.

27 H.-J. Werner and W. Meyer, *The Journal of Chemical Physics*, 1980, **73**, 2342–2356.

28 H.-J. Werner and W. Meyer, *The Journal of Chemical Physics*, 1981, **74**, 5794–5801.

29 H.-J. Werner, *Advances in Chemical Physics: Ab Initio Methods in Quantum Chemistry Part 2*, 1987, **69**, 1–62.

30 P. J. Knowles and H.-J. Werner, *Chem. Phys. Lett.*, 1988, **145**, 514.

31 H.-J. Werner and P. J. Knowles, *J. Chem. Phys.*, 1988, **89**, 5803.

32 P. J. Knowles and H.-J. Werner, *Theor. Chim. Acta*, 1992, **84**, 95.

33 E. R. Davidson and D. W. Silver, *Chem. Phys. Lett.*, 1977, **52**, 403.

34 M. Douglas and N. M. Kroll, *Annals of Physics*, 1974, **82**, 89–155.

35 B. A. Hess, *Physical Review A*, 1985, **32**, 756.

36 B. A. Hess, *Physical Review A*, 1986, **33**, 3742.

37 H.-J. Werner, P. J. Knowles, G. Knizia, F. R. Manby, M. Schütz *et al.*, *MOLPRO, version 2012.1, a package of ab initio programs*, 2012, see http://www.molpro.net.

38 A. Karton and J. M. L. Martin, *Theoretical Chemistry Accounts*, 2006, **115**, 330–333.

39 *Progress in Atomic Spectroscopy: Part A (Physics of Atoms and Molecules)*, ed. H. K. Wilhelm Hanle and H. J. Beyer, Springer, 1978.

40 W. Happer, in *Cascade and Stepwise Laser Spectroscopy of Alkali Atoms*, ed. G. zu Putlitz, E. W. Weber and A. Winnacker, Springer US, Boston, MA, 1975, pp. 651–682.

41 R. Gupta, S. Chang, C. Tai and W. Happer, *Phys. Rev. Lett.*, 1972, **29**, 695–698.

42 K. H. Liao, L. K. Lam, R. Gupta and W. Happer, *Phys. Rev. Lett.*, 1974, **32**, 1340–1343.

43 K. Hirano, K. Enomoto, M. Kumakura, Y. Takahashi and T. Yabuzaki, *Phys. Rev. A*, 2003, **68**, 012722.

44 M. Zbiri and C. Daul, *J. Chem. Phys.*, 2004, **121**, 11625.

45 A. Chattopadhyay, *Journal of Physics B: Atomic, Molecular and Optical Physics*, 2012, **45**, 035101.

46 S. H. Patil, *The Journal of Chemical Physics*, 1991, **94**, 8089–8095.

47 D. Cvetko, A. Lausi, A. Morgante, F. Tommasini, P. Cortona and M. G. Dondi, *The Journal of Chemical Physics*, 1994, **100**, 2052–2057.

48 J. Dhiflaoui, M. Bejaoui and H. Berriche, *The European Physical Journal D*, 2017, **71**, 331.

49 U. Kleinekathöfer, K. Tang, J. Toennies and C. Yiu, *Chemical Physics Letters*, 1996, **249**, 257 – 263.

50 F. Bouhadjar, K. Alioua, M. T. Bouazza and M. Bouledroua, *J. Phys. B: At. Mol. Opt. Phys*, 2014, **47**, 185201.